AUTOMATED ANALYSES OF THREE-DIMENSIONAL COMPOSITE UNIT CELLS

R. Collar, R. Wentorf, M. S. Shephard, J. Fish, Y. Qu, K.-L. Shek
Scientific Computation Research Center
Rensselaer Polytechnic Institute
Troy, NY 12180–3590

Abstract—This paper describes automated tools for the analysis of three-dimensional composite unit cells *via* the finite element method. These tools include an automated matched mesh generation algorithm, a constituent mesh volume fraction adjustment algorithm, and an iterative solver with efficient handling of the multiple right hand sides necessary for homogenization analyses. The described algorithms are used to examine the effect of the constituent volume fractions on the homogenized material properties. The local stresses within a representative composite weave are also examined.

1. Introduction

Effective design with composite materials requires the ability to predict their behavior. This behavior is partially influenced by the configuration of the constituents and other small scale features such as microcracks and voids. This paper is concerned with general automated methods allowing materials researchers and composite designers to understand the effects of constituent geometric configurations on the functions which the material must perform (*e.g.* support loads, resist deflection, transfer heat, or reflect radiation).

The large number of complex small-scale interactions in composites makes the complete characterization of the overall behavior of composites for all permutations of manufacturing and operation variables impractical. This has led to the development of multi-scale approaches where overall composite properties are derived from smaller-scale (more detailed) models of the constituents, and the effects of overall loadings are transformed into effects on the constituents. As shown in Figure ?, the small-scale modeling process begins with the definition of constituent phases and their significant features, the constitutive model(s) and associated property parameters of the solid phases, and the boundary conditions needed for the analysis. The constituent geometric features may be given either directly as idealized geometric features, e.g. cylindrical fibers, whose size and position are controlled by parameters [?, ?] or by scanned sample data with given discretization, noise processing and interpretation parameters [?]. The constitutive model is chosen based upon the material constituents, the environment, loading and expected lifetime and the tested property parameters obtained. The boundary conditions depend on the formulation of the subsequent analysis.

may be given either directly as idealized geometric features, e.g. cylindrical fibers, whose size and position are controlled by parameters [29, 23] or by scanned sample data with given discretization, noise processing and interpretation parameters [16]. The constitutive model is chosen based upon the material constituents, the environment, loading and expected lifetime and the tested property parameters obtained. The boundary conditions depend on the formulation of the subsequent analysis.

After a representative model has been developed, an analytical or numerical solution technique is employed to calculate the average material properties and constituent stress concentrations. These approaches include analytical methods based on elasticity theory for classical shapes (ellipsoids or circular fibers) included in infinite media. Such methods are the Mori-Tanaka method [19], which entails a closed form solution, the Self Consistent method [15], which entails numerical root finding, differential schemes [20], which entail solving ordinary differential equations, composite moduli bounding methods [13], and methods based on transformation strains [6]. These methods are characterized by quick solution times, do not require complicated model generating procedures, and require only material design parameters such as volume fractions and linear elastic moduli as input. However, they are limited to specific inclusion geometries.

Numerical methods for solving unit cell problems are applicable to general constituent geometries, and may be utilized wherever periodicity assumptions are valid (*i.e.* in portions of the large-scale problem domain which are not near boundaries or regions of high stress gradients). In regions of the large-scale problem domain where assumptions about the periodicity of the solution are not valid, localized approaches such as multigrid techniques [8] can be utilized. In areas of the large-scale model where periodicity assumptions are valid the homogenization technique allows for great flexibility in the choice of the included small-scale features, but at the expense of complicated model building and meshing procedures and more computationally intensive solutions. The generation of valid finite element meshes [26, 22] within the problem domain is critical to the success of these analyses. The topological and geometrical complexity of three-dimensional woven composite unit cells, and the need to analyze multiple unit cell models to optimize microstructure for a given application make the ability to generate meshes without user intervention a practical necessity. The difficulties inherent in generating three dimensional finite element meshes of geometrically complex domains may be greatly simplified by employing digital image based finite element techniques, as done by Hollister and Kikuchi [16]. This method has been shown to provide good results for the homogenization analyses they were performing, but the poor geometric representation of material interfaces does not directly permit reliable computation of local stresses near constituent boundaries. In reference [2] Dasgupta *et. al.* determine the thermal and thermo-mechanical properties of a woven composite using discretizations which provide

a smoother representation of constituent boundaries. However, meshes and results are shown for only a plain weave, and their modeling and discretization algorithms do not appear to be applicable to more complicated weave patterns. The unit cell model may also be used to determine the local stresses in the woven composite, as shown by Whitcomb *et. al.* [30] in two dimensions.

The large number of equations resulting from the numerical modeling of three-dimensional unit cells requires an efficient solution technique. The practical value of detailed unit cell representations in the design process is very limited if the computational cycle for analyzing a single microstructure entails more than a couple of hours. Application of direct equation solution methods, including state-of-the-art multifrontal solvers, is inappropriate due to the very dense structure of the stiffness matrix. However, the use of standard iterative methods is questionable due to poor conditioning caused by strong heterogeneities and anisotropies. Moreover, the need for analyzing unit cell models for multiple forcing functions (6 in classical homogenization, 24 in higher order homogenization theory [10]) further complicates the efficient utilization of iterative methods. In this paper a multilevel solution technique developed in [9, 11] is utilized for solving the linear systems of equations arising from complex microstructures.

This paper describes a set of automated finite element modeling procedures for performing homogenization analyses of woven composite unit cells. Sections 2 through 4 detail the description of the unit cell model, the generation of matched meshes on opposing faces of the unit cell, and a procedure for controlling the unit cell constituent volume fractions. Section 5 describes the solver features aimed a efficiently handling poorly conditioned linear systems subject to multiple right hand sides. Section 6 discusses the calculation of homogenized stiffness parameters, and section 7 discusses the determination of local stress values in the unit cell models. Closing remarks are made in section 8.

2. Unit Cell Model Description

The definition of the geometry of the unit cell representing the chosen composite weave geometry is needed as input to the automated unit cell analysis. The overall shape of the unit cell is a rectangular prism. Boundary conditions and other analysis attributes are associated with this basic model. For example, homogenization analysis requires that the displacement fields vary identically over opposing faces of this prism [14]. However, geometric model creation and mesh generation operations must be performed with respect to the geometry of the constituents of the weave structure. This weave structure is complex, and may be comprised of matrix, fiber bundle, and void geometries as shown in Figure 2, and may also contain cracks in the matrix material. Consideration of both the basic unit cell model and the geometric model of the weave geometry components is

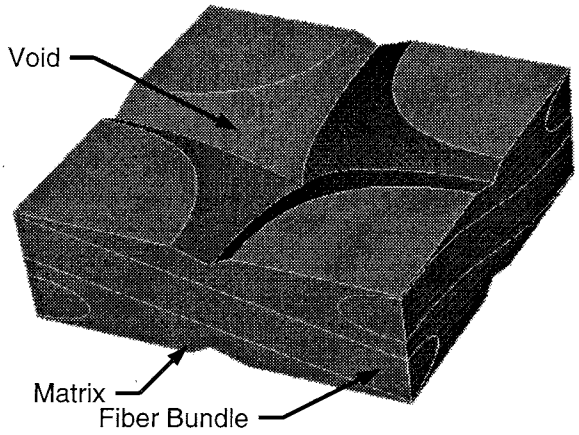

Figure 2. Typical composite weave with fiber bundles, matrix, and void geometries.

necessary in the modeling and analysis process. The weave characteristics and analysis attributes of the composite being modeled may be altered to optimize the composite as shown in Figure 3.

The schematic in Figure 3 depicts the inputs and outputs (arcs) for each function (boxes) used to implement the automated homogenization "Solution Technique" of Figure 1. The "Geometric Modeler" (top of Figure 3) provides a non-manifold boundary representation [18] of the composite weave geometry comprising the unit cell. This representation is comprised of both topology, which describes the relationships of the model entities, and geometry, which describes the shape of the model entities.

The "Matched Mesher" function (middle right of Figure 3) uses the geometric model information and constraints dictated by the periodic boundary conditions to automatically create a three-dimensional mesh of the composite weave. A set of "Mesh Copy Operations" is used to create matching surface mesh topology and geometry on opposing faces of the unit cell. The mesh matching requirements are specified *via* the rectangular prism "Unit Cell Template" (middle left of Figure 3), and are independent of the composite weave geometric model. The topology of the composite weave geometric model is associated with the topology of the unit cell template by the "Classify on Unit Cell" function shown in Figure 3. After the mesh has been generated, mesh queries and manipulations are performed *via* the "Generic Mesh Database Operations" [1] indicated on the right side of Figure 3.

The unit cell template is also used to automatically "Identify Moveable Constituent Topology", as indicated in the center of Figure 3. This function determines the topological entities of the given "Target Constituents" in the composite weave model for which the associated mesh may be altered to "Adjust Constituent Mesh Volumes" to the given "Target Volume Fractions" by the subsequent function shown in Figure 3.

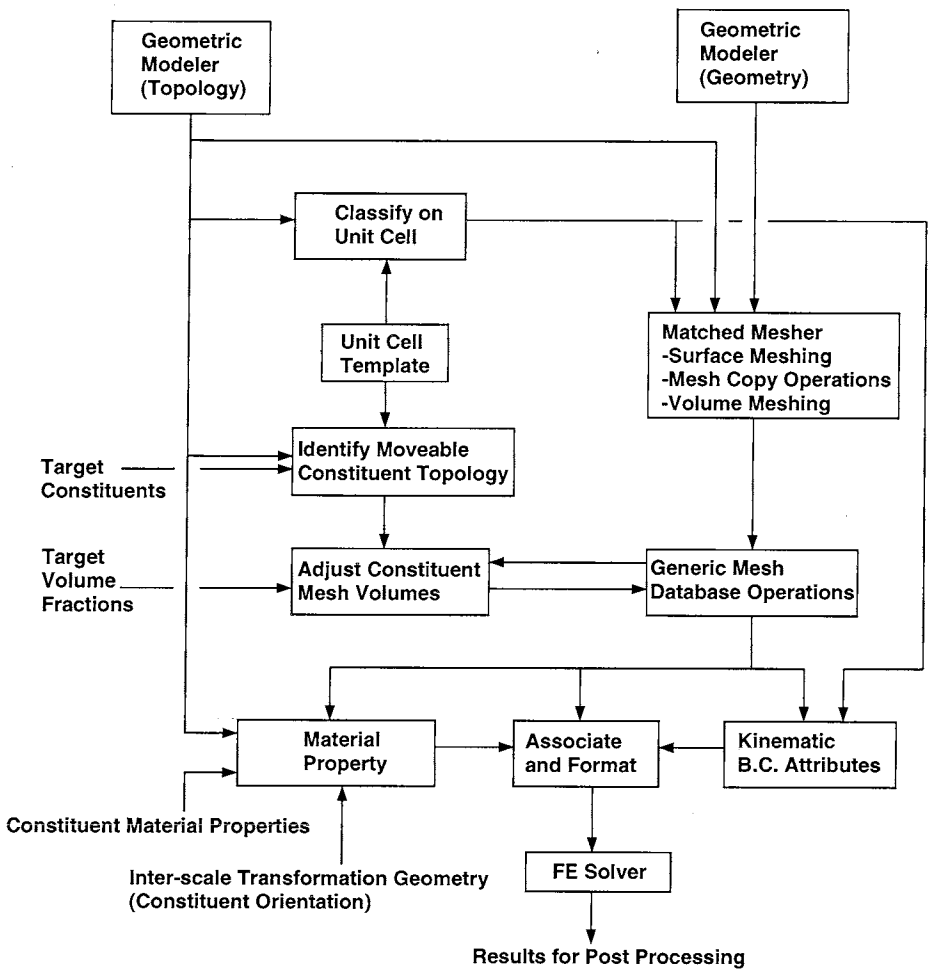

Figure 3. Details present in the automated finite element based homogenization analysis of composite unit cells.

The "Material Property" function (lower left of Figure 3) forms the constitutive relations for each constituent in the composite. The necessary constituent material properties are selected from a relational material property database indexed by compound, form, manufacturer, environment, or other factors. Alternatively, the properties are computed from a lower scale analysis of the average properties of micro-constituents. Complete definition of material properties also requires inter-scale transformation geometries to provide local coordinate systems orienting non-isotropic material models. Data from the geometric modeler is used to associate the material properties (and other analysis attributes [24]) with the geometric model topology. Associating these properties with the geometric model makes them independent of the mesh, and the mesh can therefore be altered without requiring their respecification.

The "Kinematic B.C. Attributes" function (lower right in Figure 3) specifies the appropriate boundary conditions for the homogenization analysis. These attributes and the constitutive relations are associated with the correct finite element mesh entities and formatted as necessary for the finite element solver by the "Associate and Format" function shown at the lower center of Figure 3. The resulting system of equations is provided to the finite element solver ("FE Solver" at the bottom of Figure 3), and the resulting solution data is supplied to appropriate post processing routines.

3. Matched Mesh Generation

Since the homogenization modeling is performed *via* the finite element method, the necessary periodic boundary conditions are specified to the equation solver in terms of nodal displacement requirements (multi-point constraints). Since the displacement solution field is not constant over a cell face, the displacement of a given node, referred to as the subordinate node, on one face of the unit cell is defined as a function of the displacements of specific nodes, referred to as control nodes, on the opposing unit cell face. That is

$$\underline{u}_i = \sum_{j=1}^{N_{con}} a_j \underline{u}_j \tag{1}$$

where $\underline{u}_i$ denotes the displacements of the i^{th} subordinate node, $\underline{u}_j$ denotes the displacements of the j^{th} control node, a_j are weighting values, and N_{con} is the number of control nodes associated with the current subordinate node. The displacement function for a given node is written in terms of the shape functions of the element face which contains the projection of the given node on the opposing unit cell face, as shown in Figure 4. This approach requires an expensive search process to determine within which element faces the projected node lies. The projected point must also be located in the parametric (ξ_1, ξ_2, ξ_3) space of the element face to express the displacement of the

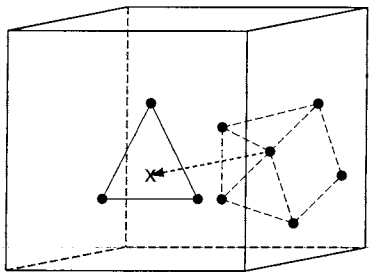

Figure 4. Projection of node from back face of unit a cell to an element face on the opposing unit cell face.

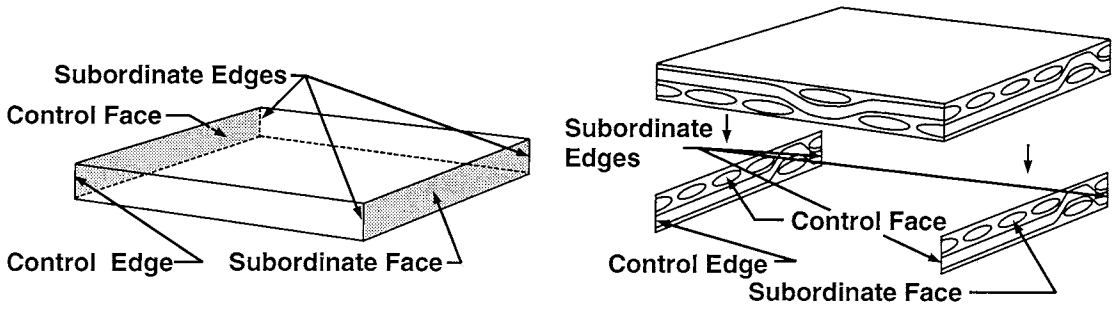

(a) (b)

Figure 5. Determining control-subordinate relationships for the weave geometric model. (a)Typical relationships on the unit cell template. (b)Corresponding relationships on the weave geometric model.

subordinate node in terms of the control nodes. The complexity of this calculation is increased if higher order polynomial element geometry interpolations are utilized.

Specification of the periodic boundary conditions is substantially simplified if the finite element nodes on opposing unit cell faces match. In this case the periodic boundary condition for a given subordinate node reduces to

$$\underline{u}_i = \underline{u}_j \tag{2}$$

where $\underline{u}_j$ is the displacement of the sole control node. With *a priori* knowledge of the correspondence between nodes on opposing faces of the unit cell, no searching is required and it is not necessary to locate a projected point in real space within the parametric space of an element face.

Matched meshes are generated by first discretizing the weave geometric model outer boundary entities which are defined as "control" entities, and then copying the meshes to the matching "subordinate" weave geometric model entities. In order to generate a matched mesh of the weave geometric model, it is therefore necessary to identify the control-subordinate relationships of the weave geometric model outer boundary topological entities. For convenience, the outer boundary of the weave geometric model is denoted as ∂M. The control-subordinate relationships are determined by associating the topological entities of ∂M with the predetermined control and subordinate topology of the unit cell template.

One unit cell template face of each opposing pair of faces is specified as the control face, and the other is specified as the subordinate face. One of the three such pairs of faces is indicated on the unit cell template shown in Figure 5(a). Periodicity in each

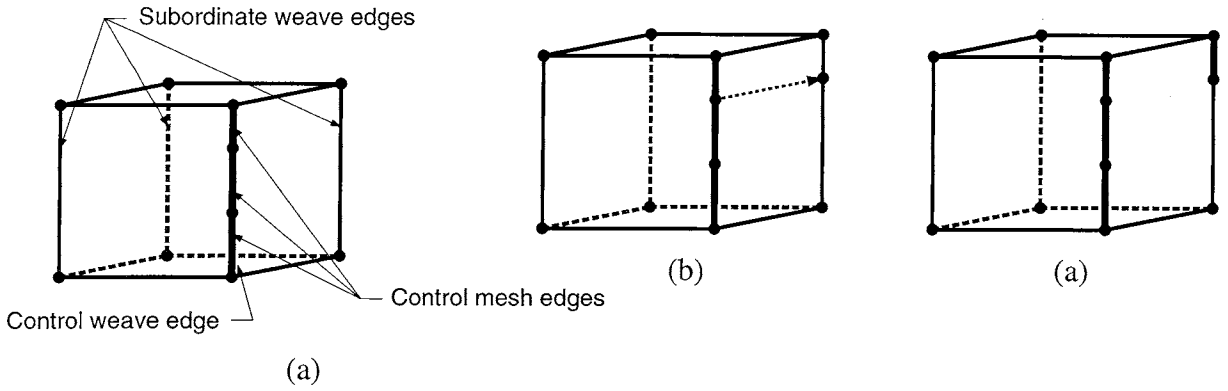

Figure 6. Edge meshing procedure. (a)Control edge is meshed. (b)Mesh vertices from control edge are copied to subordinate weave edge. (c)New mesh edge is created on subordinate weave edge.

direction normal to the faces of the unit cell requires that parallel edges of the box-shaped unit cell template undergo the same variations in displacement and must have identical meshes. One unit cell template edge in each group of four parallel edges is specified as the control edge, and the other three are designated as subordinate edges. One of the three such control-subordinate edge groups is shown in Figure 5(a). All eight vertices of the unit cell undergo the same displacement, and (trivially) must have identical meshes.

Each ∂M face associated with a control face of the unit cell template is identified as a control face, and the matching ∂M face is identified as a subordinate face, as shown for a typical pair of weave geometric model faces in Figure 5(b). If a ∂M edge lies within a control face of the unit cell template, then it has one matching ∂M edge lying within the opposing subordinate face of the unit cell template. If a ∂M edge lies on a control edge of the unit cell template, it has three matching edges lying on the parallel subordinate edges of the unit cell template, as shown for one group of ∂M edges in Figure 5(b). The ∂M vertices similarly inherit control-subordinate designations.

Generating meshes in a hierarchic manner (*i.e.* meshing vertices first, then edges, faces, and volumes) allows the periodicity requirements to be easily satisfied during the meshing process, since discretizing the weave geometric model face boundaries first ensures that the necessary matching meshes can be generated in their adjacent faces.

The control ∂M edges are meshed first, as shown in Figure 6(a). As described in reference [3], the edge meshing is done such that the resulting discrete edges are of approximately the same size as requested by the user. The meshes on the control edges are then copied to the subordinate weave edges. This is done by first creating a new subordinate mesh vertex as shown in Figure 6(b). A new mesh edge is then created and

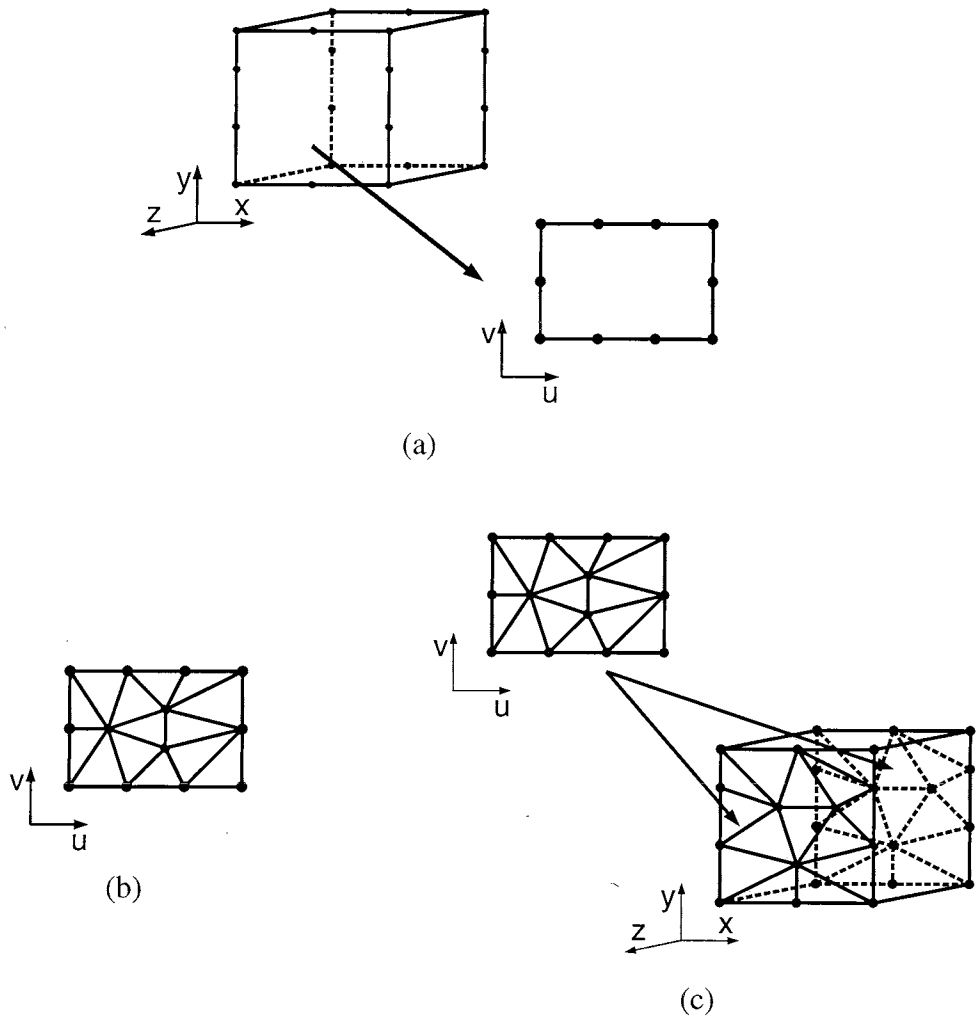

Figure 7. Weave Face meshing. (a)Boundary mesh is copied into the parametric space. (b)Delaunay insertion method is used in the parametric space. (c)Face mesh is copied back into the real space.

classified on the subordinate weave edge, as shown in Figure 6(c).

The weave faces are then meshed by a surface meshing algorithm which discretizes the model faces in their parametric spaces [3]. The weave face boundary mesh is first copied into the parametric space, as shown in Figure 7(a). The surface mesh is then created using a Delaunay insertion method as illustrated in Figure 7(b). After the surface mesh has been created in the parametric space, it is copied back to the weave face in the real space by obtaining the corresponding xyz coordinates for each of the mesh vertex

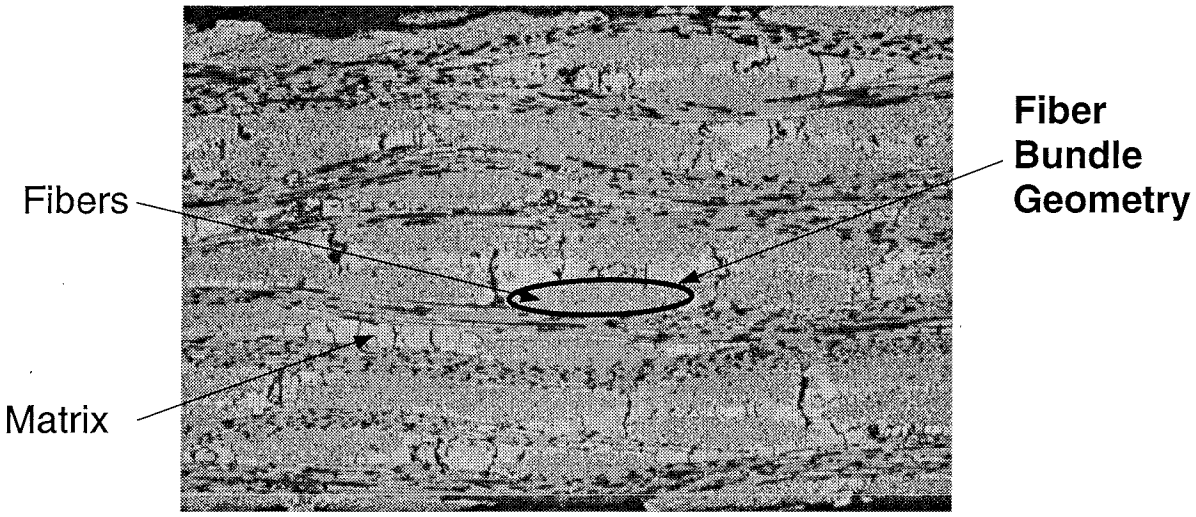

Figure 8. Micrograph of a planar weave composite.

parameter values as shown in Figure 7(c). The matching mesh on the subordinate weave face is created by also copying the temporary mesh to the corresponding subordinate weave face.

The region meshing process is comprised of three steps [5, 25]. In the first step an underlying variable level octree is created to reflect mesh size control information during the region meshing procedure. The octants residing far enough inside the model interior are then meshed using templates. Finally, a face removal procedure is used to connect the surface triangulation to the interior elements.

4. Control of Constituent Volume Fractions

The efficiency of the analysis process is increased by using the fewest number of degrees of freedom which can achieve the desired accuracy for the requested parameters. In finite element analyses the solution accuracy is affected by both discretization error and geometric approximation error. Discretization error is caused by the projection of the solution field into a finite dimensional space. If this error is dominant, then the discretization must be suitably refined to improve solution accuracy.

Geometric approximation error is caused by the piecewise approximation of curved model geometry. The presence of curved geometries in composite microstructures is illustrated by the cross-sectional view of a planar weave composite shown in Figure 8. The matrix and fiber bundle geometries are clearly visible in this image, as are the individual fibers comprising the fiber bundles. The weave geometric models presented in this paper consist of fiber bundle and matrix constituents only. The smaller-scale

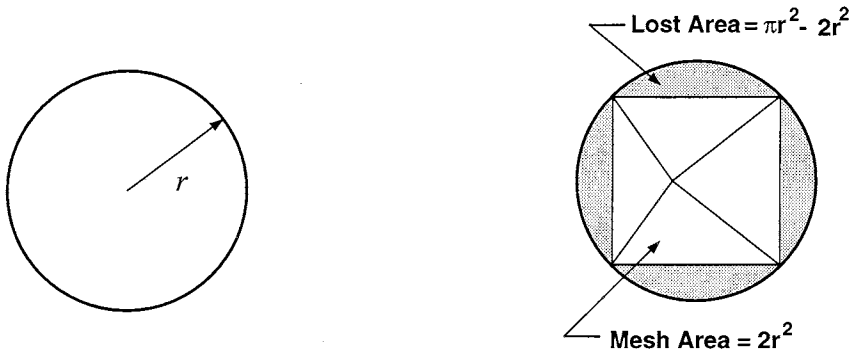

Figure 9. Mesh volume error example. (a)Circular geometric model of radius r. (b)Inscribed mesh.

modeling of the fibers within the bundles is done *via* the Mori-Tanaka method. Since the fiber bundles are convex in cross-section and are curved to form the weave, geometric approximation creates errors in the constituent volume fractions calculated from the finite element mesh. The mesh constituent volume fractions, C_c^{FE}, are defined as

$$C_c^{FE} = \frac{V_{cons}^{FE}}{V_{cell}} \tag{3}$$

where V_{cons}^{FE} is the volume of the elements classified inside the constituent regions of the geometric model, and V_{cell} is the total volume of the unit cell. The errors in the mesh volume fractions can be sizeable, as illustrated by the circular geometric model of radius r in Figure 9(a). The circle is discretized such that there are four finite element mesh edges of equal length around the circumference as shown in Figure 9(b), and each edge is of length $\sqrt{2}r$. The resulting mesh area is $2r^2$, and the "lost" area not contained within the mesh is $\pi r^2 - 2r^2$, as indicated by the shaded portions of Figure 9(b). The area error of the mesh is therefore -36%.

In homogenization analyses, the results presented here indicate that the C_c^{FE} values influence the evaluation of the homogenized material parameters more strongly than does the discretization error. The C_c^{FE} errors must therefore be reduced to improve the analysis accuracy. There are several methods by which these errors may be reduced. The simplest method consists of refining the mesh to improve the approximation of the model geometry. This process dramatically increases the number of degrees of freedom in the domain, as illustrated by the meshes of a base one planar weave geometric model shown in Figure 10. Only the mesh faces classified on the interior fiber bundle surfaces are

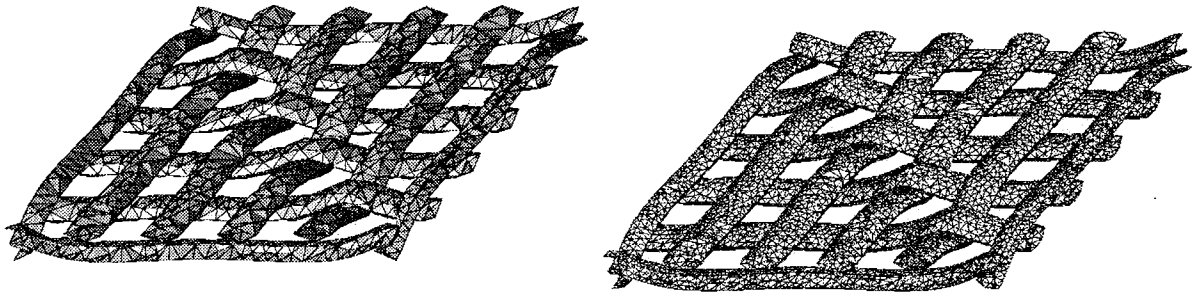

(a) (b)

Figure 10. Solid mesh of base one planar weave model. Only mesh faces on interior bundle surfaces are shown. (a)Coarse mesh of 21,850 elements. (b)Fine mesh of 154,020 elements.

shown in these figures. The mesh in Figure 10(a) contains 21,850 elements and 4,608 nodes. The mesh fiber bundle volume fraction, C_b^{FE}, of this mesh is 0.2527, which is in error by -19.4% when compared to the geometric model fiber bundle volume fraction of 0.3137. The mesh in Figure 10(b) was created through uniform refinement and contains 154,020 elements and 28,858 nodes. The fiber bundle volume fraction is 0.298761, which is in error by –4.8%. The approximation of the fiber bundle volume fraction by the finite element mesh improved, but still underestimates the fiber bundle volume fraction of the geometric model, and the number of degrees of freedom in the domain increased by a factor of greater than 6. The memory requirements and large increases in solution time for the highly refined meshes needed to adequately approximate the fiber bundle volume fraction make this an expensive method.

Another approach for reducing the errors in C_c^{FE} values entails making adjustments to the geometric model such that the constituent volume fractions of the geometric model are higher than the constituent volume fractions of the actual composite material. The constituent volume fractions of the finite element mesh generated within this model then more closely approximate the constituent volume fractions of the composite material. This method requires iterations of the model construction and mesh generation processes to reduce the C_c^{FE} errors to a given level. Further, since C_c^{FE} values are a function of discretization size, meshes of different degrees of refinement require the construction of different geometric models to obtain the same C_c^{FE} values.

The chosen method for reducing the C_c^{FE} errors involves the modification of an existing mesh. This method begins with an initial mesh which is valid and of acceptable element shape quality, and relocates the mesh vertices classified on the surfaces of the constituents under consideration to correct C_c^{FE} values of those constituents. The mesh vertices are relocated in a manner such that the validity and quality of the mesh is

maintained. In the current implementation, the quality of the mesh is measured by the largest dihedral angle [17]. Although this C_c^{FE} adjustment method is an iterative procedure, it does not require the creation of a new finite element mesh for each iterative step. Instead, the same mesh topology is used throughout the process with changes being made only to the locations of specific mesh vertices.

The values of the desired mesh bundle volume fraction, $\overline{C}_b$, and the bundle volume fraction of the existing mesh, C_b^{FE}, are utilized to determine how the mesh should be altered. Since the area A of an ellipse is given by [27]

$$A = \int r(\theta)^2 d\theta \tag{4}$$

where r is the distance from the bundle centerline to a point on the bundle surface and θ is the angular measure around the ellipse, the volume of a given fiber bundle is proportional to the square of the radius of the elliptical bundle cross-section

$$V_b \propto r^2(\theta, s) \tag{5}$$

where V_b is the volume of the bundle, and s is a parametric measure along the bundle centerline. Using equation (5), the new bundle radius R required to achieve the desired fiber bundle volume $\overline{V}_b$ is expressed as

$$R(\theta, s) \propto \sqrt{\overline{V}_b} \tag{6}$$

The new bundle radius R is therefore calculated as a function of the current bundle radius

$$R(\theta, s) = \sqrt{\frac{\overline{V}_b}{V_b}}\, r(\theta, s) \tag{7}$$

If all of the fiber bundles in the geometric model are of the same cross-sectional geometry, equation (7) may be expressed in terms of the volume fraction measures $\overline{C}_b$ and C_b^{FE}

$$R(\theta, s) = \Phi\, r(\theta, s) \tag{8}$$

where $\Phi = \sqrt{\overline{C}_b / C_b^{FE}}$ is the bundle volume adjustment factor.

The new position of each mesh vertex on the bundle surfaces is calculated as a function of the bundle volume adjustment factor, Φ, as illustrated for a typical ellipsoidal bundle cross-section in Figure 11. The current positions $\underline{x}_i$ of the vertices in the inscribed surface discretization of the bundle cross-section are located distances r_i from the center of the bundle cross-section, as shown in Figure 11(a). If the bundle volume adjustment factor is greater than one, each of the mesh vertices is located radially outward from

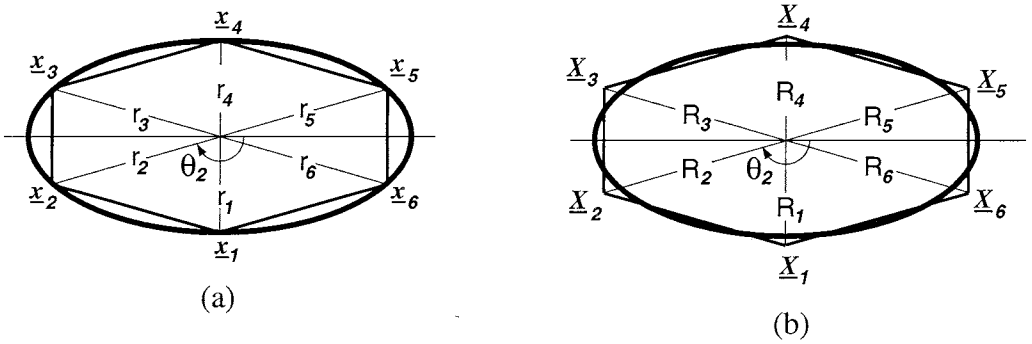

Figure 11. Cross section of an ellipsoidal fiber bundle. (a)Inscribed discretization, and distance to mesh vertex. (b)Distance to relocated vertex.

its current position to its new location $\underline{X}_i$ at a distance R_i from the bundle center, as shown in Figure 11(b). The coordinates to which the vertex is relocated are therefore calculated as

$$\underline{X} = \underline{x} + (\Phi - 1)\underline{r} \tag{9}$$

where $\underline{r}$ denotes the vector from the bundle center to the current location of the vertex. Scaling the bundle cross-section by Φ in this manner maintains the original shape of the bundle cross-section, as can be seen by examining the aspect ratios of the ellipses in Figure 11. The aspect ratio α_I of the original discretization is calculated as

$$\alpha_I = \frac{r_1}{r_2 \cos\theta_2} \tag{10}$$

and the aspect ratio α_{II} of the adjusted discretization is calculated as

$$\alpha_{II} = \frac{R_1}{R_2 \cos\theta_2} \tag{11}$$

Substitution of equation (8) in equation (11) results in

$$\alpha_{II} = \frac{r_1}{r_2 \cos\theta_2} \tag{12}$$

After moving a given vertex to the new position determined from equation (9), the validity and quality of the mesh is evaluated. If any of the dihedral angles affected by the vertex movement exceed the largest dihedral angle in the original mesh, a new vertex position is determined by bisecting the distance the vertex was moved and again checking the quality of the mesh. The vertex relocation procedure is repeated until a location is

found for which the mesh quality does not degrade. The vertex is returned to its original location if after five distance bisections no location can be found for which the quality of the mesh does not degrade. This process permits the bundle surface mesh to be altered anisotropically if the movement of mesh vertices is constrained in some manner. Such constraints are caused by the proximity of geometric model entities, or by the topology and geometry of the mesh surrounding the fiber bundle surface.

After the mesh vertices on the bundle surfaces have been moved to their new positions, a constrained Laplacian smoothing [7], utilizing a specific element shape parameter [4], is employed to improve the shapes of the altered elements. The surface and edge smoothing techniques usually employed in automatic mesh generation algorithms would pull the vertices classified on the bundle surfaces back to the surfaces of the geometric model, thereby restoring the original constituent mesh volume fractions. Therefore, in the current implementation only the mesh vertices classified on the interior of the geometric model regions are subjected to smoothing operations.

The following example demonstrates the ability of the algorithm to adjust C_b^{FE} to a prescribed value. The geometric model for this example was created with the Shapes^{TM} [31] geometric modeler. The example consists of a unit cell containing a single cylindrical fiber bundle. The unit cell is of height $h = 2$, width $w = 2$, and length $l = 5$. The fiber bundle is of radius $r = 0.5$. The exact bundle volume fraction, $\overline{C}_b$, is 0.19635. The initial mesh of the unit cell model is shown in Figure 12. The exterior of the mesh is shown in Figure 12(a), and the interior mesh faces on the surface of the fiber bundle are shown in Figure 12(b). The C_b^{FE} of this mesh is 0.13421, which represents a -31.6% error. The mesh volume fraction correction algorithm was then used to adjust the mesh to the correct bundle volume fraction. The exterior faces of the adjusted mesh are shown in Figure 12(c), and the interior mesh faces classified on the surface of the bundle are shown in Figure 12(d). In this case the topology and geometry of the volume mesh outside of the bundle region prevented some mesh vertices from moving to the full extent of the relocation prescribed by the volume fraction adjustment algorithm without degrading the mesh quality. Three iterations of the mesh volume fraction correction procedure were required to raise the bundle volume fraction to within 1% of $\overline{C}_b$. The value of the mesh volume fraction at the end of each of the three iterations is listed in Table 1. Section 6 contains examples of composite weave geometries where similar improvements were obtained.

5. Iterative Solution of Unit Cell Problems

The Generalized Aggregation Method (GAM) is utilized for solving the unit cell problems. These problems are characterized by a large system of linear equations with

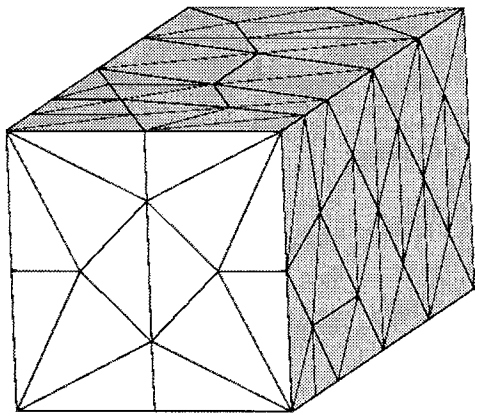

(a)

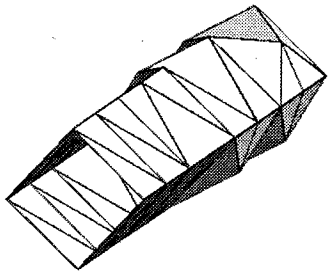

(b)

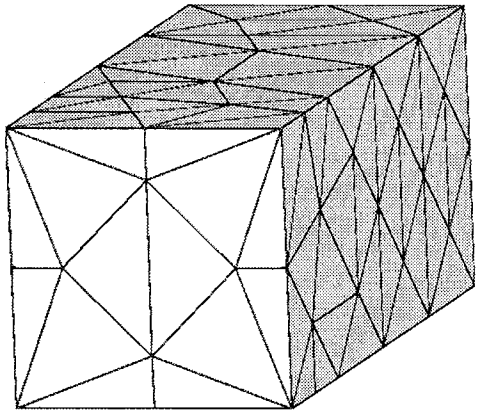

(c)

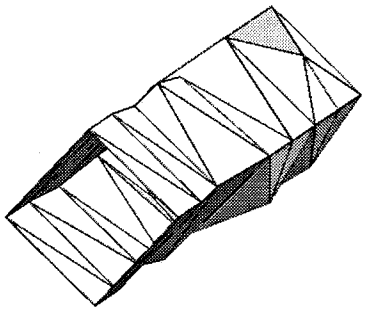

(d)

Figure 12. Single fiber bundle example meshes. (a)Exterior mesh faces of initial mesh (31.6% bundle volume fraction error). (b)Initial mesh faces classified on interior fiber bundle surface. (c)Exterior mesh faces of adjusted mesh (-0.3% bundle volume fraction error). (d)Adjusted mesh faces classified on interior fiber bundle surface.

multiple right hand sides and multi-point constraints, and may be written as

$$\underline{Q}^T \underline{\hat{K}} \underline{Q} \underline{u}_m = \underline{Q}^T \underline{f} \tag{13}$$

where $\underline{\hat{K}}$ is the unit cell stiffness matrix, $\underline{f}$ is a forcing matrix given by

$$\underline{f} = -\int_\theta \underline{B}^T \underline{D} d\theta \tag{14}$$

Mesh Move Iteration	Mesh Bundle Volume Fraction (desired = 0.19635)	Mesh Bundle Volume Fraction Error (%)
initial mesh	0.13421	-31.6
1	0.18209	-7.3
2	0.19369	-1.3
3	0.19579	-0.3

Table 1. Mesh bundle volume fraction and percent error at each iteration of the volume fraction correction of the single fiber bundle example.

$\underline{B}$ is a strain-displacement matrix, θ is the unit cell domain, $\underline{D}$ is the small-scale constitutive tensor, and $\underline{Q}$ is the multi-point constraint matrix relating the control degrees of freedom $\underline{u}_c$ to the set of all degrees of freedom $\underline{u}$ as

$$\underline{u} = \underline{Q}\underline{u}_m \tag{15}$$

Further details are contained in [9].

5.1 Solver Description

GAM is a multilevel solution scheme based on the multigrid philosophy, which captures the lower frequency response by solving an auxiliary coarse model, whereas the higher frequency response is resolved by smoothing on the source grid. As such GAM possesses an optimal rate of convergence by which the CPU time grows linearly with the problem size. Unlike the multigrid method GAM does not require construction of auxiliary grids. Furthermore, because of the adaptive control of the structure of the preconditioner GAM is insensitive to problem conditioning in terms of number of iterations. In GAM the auxiliary coarse model is directly constructed from the source grid by decomposing the whole set of nodes into non-intersecting blocks to be referred to as aggregates, and then for each aggregate assigning a reduced number of degrees of freedom. By doing so one reduces the dimensionality of the source problem, while maintaining the compatibility of the solution. Theorems quantifying the optimal approximation properties aimed at ensuring that the coarse model will effectively capture the lower frequency response of the source system and at the same time will be sparse and rapidly computed have been described in [9].

5.2 Multiple Right Hand Sides

A combination of two mechanisms is employed to provide a rapid solution for linear systems of equations (13) with multiple right hand sides:

1. Construction of the preconditioner aimed at reducing the overall cost of the iterative process at the expense of increasing the computational cost of computing the preconditioner;
2. Acceleration of the GAM scheme with the block conjugate gradient method.

5.2.1 GAM Preconditioner for Problems with Multiple Right Hand Sides

One of the key aspects of the GAM scheme is a selection of the coarse model cut-off frequency parameter γ, below which all the eigenvectors of the eigenvalue problem on the aggregate are included within the prolongation operator. In order to make this parameter dimensionless, the eigenvalue problem on each aggregate a is formulated in the following manner:

$$\underline{K}^a \underline{\phi}^a = \lambda^a \underline{D}^a \underline{\phi}^a \tag{16}$$

where $\underline{D}^a$ is the diagonal of $\underline{K}^a$.

The value of the parameter γ determines the effectiveness of coarse grid correction. In the limit as $\gamma \rightarrow \max_a \lambda^a$, the auxiliary problem captures the response of the source system for all frequencies and therefore the two-level procedure converges in a single iteration even without smoothing. On the negative side, for large values of γ, the eigenvalue analysis on each aggregate becomes prohibitively expensive and the auxiliary matrix becomes both large and dense. At the other extreme, in the limit as $\gamma \rightarrow 0$ the prolongation operator contains the rigid body modes of all the aggregates only, and thus the auxiliary problem becomes inefficient for ill-posed problems.

For problems with multiple right hand sides the value of γ should be increased to reduce the number of iterations, and consequently to reduce the overall computational cost.

5.2.2 Block Conjugate Gradient Accelerator

The system of linear equations with s load cases given in (13) can be expressed in a block structure as

$$\underline{K}\,\underline{U} = \underline{F} \tag{17}$$

where $\underline{U} = [\underline{u}_1, \underline{u}_2, \ldots, \underline{u}_s]$, $\underline{F} = \left[\underline{f}_1, \underline{f}_2, \ldots \underline{f}_s\right]$ and $\underline{u}_i$, $\underline{f}_i$ are the i^{th} load vector and the corresponding solution, respectively. The matrix $\underline{K} \in \Re^{n \times n}$ is the global stiffness matrix which is symmetric, positive definite and sparse.

The forcing functions are orthonormalized using the Gram-Schmidt procedure to obtain $\overline{\underline{F}}(\underline{F} = \overline{\underline{F}}\,\underline{H}_m)$ and to ensure that the resulting set of forcing functions is linearly independent

$$\delta_i \overline{\underline{f}}_i^0 = \underline{f}_i^0 - \sum_{j=1}^{i-1} \gamma_j^i \overline{\underline{f}}_i^0 \qquad i = 1, \ldots, s \tag{18}$$

where

$$\gamma_j^i = \left(\overline{\underline{f}}_i^0\right)^T \underline{f}_i^0 \tag{19}$$

and δ_i is the set of parameters which normalize $\underline{f}_i$. The original problem $\underline{K}\,\underline{U} = \underline{F}$ can then be transformed into $\underline{K}\,\overline{\underline{U}} = \overline{\underline{F}}$ where $\underline{F} = \overline{\underline{F}}\,\underline{H}_m$ and $\underline{H}_m$ is an upper triangular matrix of the form:

$$\underline{H}_m = \begin{bmatrix} \delta_1 & \gamma_1^2 & \cdots & \cdots & \gamma_1^2 \\ & \delta_2 & & & \vdots \\ & & & & \vdots \\ & 0 & & \delta_{s-1} & \gamma_{s-1}^s \\ & & & & \delta_s \end{bmatrix} \tag{20}$$

The block conjugate gradient acceleration scheme described below utilizes the GAM cycle as a preconditioner. To clarify ideas consider the following energy functional

$$\underline{\Phi}(\underline{U}) = [\Phi_1(\underline{u}_1)\ \Phi_2(\underline{u}_2)\ \ldots\ \Phi_s(\underline{u}_s)] \tag{21}$$

where$\Phi_i(\underline{u}_i) = \frac{1}{2}\underline{u}_i^T \underline{K}\,\underline{u}_i - \underline{u}_i^T \underline{f}_i$. The corresponding block residual matrix $\underline{R}_i \in \Re^{n\times s}$ at the i^{th} step is $\underline{R}_i = \underline{F} - \underline{K}\underline{U}_i$ and the corresponding solution $\underline{U}_{i+1} \in \Re^{n\times s}$ is defined as

$$\underline{U}_{i+1} = \underline{U}_i + \underline{V}_{i+1}\underline{A}_i \tag{22}$$

where $\underline{V}_i \in \Re^{n\times s}$ spans the subspace of search directions, and $\underline{A}_i \in \Re^{s\times s}$ is the matrix representing the step length determined by the minimization

$$\frac{\partial \underline{\Phi}(\underline{U}_i + \underline{V}_{i+1}\underline{A}_i)}{\partial \underline{A}_i} = 0 \tag{23}$$

which yields $\underline{V}_{i+1}^T \underline{R}_{i+1} = 0$. The subspace $\underline{V}_{i+1}$ is subsequently constructed by

$$\underline{V}_{i+1} = \underline{Z}_i + \underline{V}_i \underline{B}_i \tag{24}$$

where the parameter matrix $\underline{B}_i \in \Re^{s\times s}$ is determined from the block conjugacy condition $\underline{V}_{i+1}^T \underline{K}\,\underline{V}_i = 0$, and $\underline{Z}_i$ is the predictor from a single GAM cycle. The complete algorithm is summarized below.

Step 1: Initiation

$\overline{\underline{U}}_0 = \underline{0} \qquad \underline{R}_0 = \overline{\underline{F}}$

$\underline{B}_0 = \underline{0} \qquad \underline{Z}_0 = \underline{0}$

Step 2: Do i=0, 1, . . . until all right hand sides converge

$$\underline{Z}_i = GAM(\underline{R}_i, \underline{K})$$

$$\left(\underline{R}_{i-1}^T \underline{Z}_{i-1}\right)\underline{B}_i = \underline{R}_i^T \underline{Z}_i$$

$$\underline{V}_{i+1} = \underline{Z}_i + \underline{V}_i \underline{B}_i$$

$$\underline{X}_{i+1} = \underline{K}\underline{V}_{i+1}$$

$$\left(\underline{V}_{i+1}\underline{X}_{i+1}\right)\underline{A}_i = \underline{R}_i^T \underline{Z}_i$$

$$\overline{\underline{U}}_{i+1} = \overline{\underline{U}}_i + \underline{V}_{i+1}\underline{A}_i$$

$$\underline{R}_i = \underline{R}_i - \underline{X}_{i+1}\underline{A}_i$$

Convergence is checked for each right hand side. If one of the right hand sides converges, it is removed from the iterative process. Once all the right hand sides have converged, the final solution is recovered as

$$\underline{U} = \overline{\underline{U}}\,\underline{H}_m \tag{25}$$

5.3 Multiple Point Constraints

The GAM scheme can deal with multi-point constraints in a conventional way if all the elements containing at least one "subordinate" node form a separate aggregate. Each multi-point constraint can then be represented as follows:

$$\underline{u}_s = \underline{T}\,\underline{u}_c \tag{26}$$

where $\underline{u}_s$ are the subordinate" degrees of freedom, and $\underline{T}$ is a transformation matrix representing the multi-point constraint data:

$$\underline{u} = \begin{bmatrix} \underline{T} \\ \underline{I} \end{bmatrix} \underline{u}_s = \underline{Q}\,\underline{u}_s \tag{27}$$

6. Calculation of Homogenized Stiffness Parameters

The effect of C_b^{FE} on the homogenized stiffness parameters of a composite material is easily seen in an analysis of a single bundle unit cell. This model consists of a cylindrical fiber of radius $r = 0.5$ embedded in a block of matrix of length $l = 2$, width $w = 2$, and height $h = 2$. The isotropic matrix material modulus and Poisson's ratio were chosen as

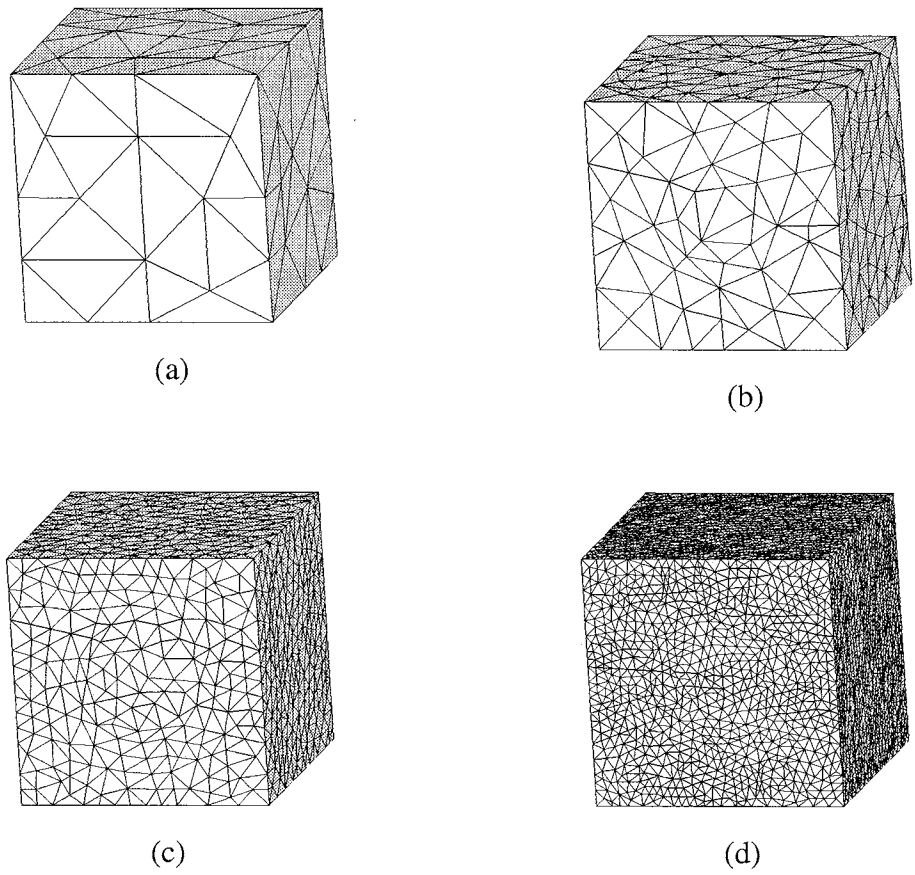

Figure 13. Finite element meshes of the single fiber bundle model. (a)93 vertices and 284 elements. (b)576 vertices and 2,549 elements. (c)4,156 vertices and 21,951 elements. (d)20,615 vertices and 110,638 elements.

6.89 msi and 0.33, which are representative of Titanium. The isotropic bundle material modulus, shear modulus, and Poisson's ratio were chosen as 37.9 msi, 15.7 msi, and 0.21 which are representative of a silicon carbide fiber.

A series of meshes of increasing levels of uniform refinement was generated, as shown in Figure 13. The coarsest mesh, shown in Figure 13(a), contains 93 vertices and 284 elements. The mesh shown in Figure 13(b) contains 576 vertices and 2,549 elements. The mesh shown in Figure 13(c) contains 4,156 vertices and 21,951 elements. The finest mesh, shown in Figure 13(d), contains 20,615 vertices and 110,638 elements. Homogenization analyses were performed with each of the four meshes, and also with the volume fractions of the four meshes corrected to within $\pm 0.5\%$ of the correct volume fraction for the geometric model.

Number of Vertices	Mesh Bundle Volume Fraction	Mesh Bundle Volume Fraction Error (%)	G_{33} ($\times 10^7$ psi)	G_{33} Difference (%)
93	0.14998	-23.61	1.4906	-8.79
93	0.18409	-6.24	1.5976	-2.24
93	0.19263	-1.89	1.6244	-0.6
93	0.19623	-0.06	1.6357	0.09
576	0.18440	-6.09	1.5972	-2.26
576	0.19351	-1.45	1.6257	-0.52
576	0.19630	-0.02	1.6345	0.02
4,156	0.19334	-1.53	1.6248	-0.57
4,156	0.19633	-0.01	1.6342	0.00
20,615	0.19558	-0.39	1.6318	-0.15
20,615	0.19635	0.00	1.6342	0.00

Table 2. Mesh bundle volume fraction and homogenized material stiffness differences for the discretizations shown in Figure 13.

The most relevant stiffness parameter for the single bundle model is the parameter corresponding to the axial stiffness of the bundle. For the model under consideration the fiber bundle axis is aligned with the z direction, making the G_{33} term of the homogenized material stiffness matrix $\underline{G}$ of greatest relevance. The values of G_{33} computed using the various discretizations were compared to G_{33} computed with the finest mesh adjusted to 0.0% bundle volume fraction error.

The percent differences between the G_{33} values and the G_{33} value of the finest mesh are listed in Table 2. This data may be examined in two manners. The first entails viewing the homogenized axial stiffness parameter differences as a function of the C_b^{FE} error. The C_b^{FE} of each mesh was adjusted to match the initial C_b^{FE} values of the finer discretizations and also to $\overline{C}_b$. The change in the value of the axial stiffness parameter for a given mesh corrected to different C_b^{FE} values shows the effect of improving the geometric approximation only. This data shows that all of the discretizations adjusted to within $\pm 0.5\%$ of $\overline{C}_b$ produced nearly the same axial stiffness parameter. In particular, the coarse discretization and the fine discretization produced results which differed by only 0.09%. This result indicates that it is possible to use coarse discretizations and achieve accurate results if the geometric approximation error is controlled. This shortens the analysis cycle since it is much quicker to generate coarse discretizations and

also much quicker to perform the homogenization analysis on the coarse discretization. The CPU time required for the mesh generation and homogenization solution of the coarse discretization was 444 times faster than the time required for the most refined discretization.

Examining the homogenized axial stiffness differences for meshes corrected to within $\pm 0.5\%$ of the same C_b^{FE} shows a small change in this parameter with increasing mesh refinement. When all the discretizations were corrected to within $\pm 0.5\%$ of $\overline{C}_b$, changing the number of mesh vertices by two orders of magnitude resulted in only a 0.09% change in the homogenized axial stiffness parameter estimate. In contrast, changing the volume fraction of the coarse discretization by less than 2% resulted in a 0.69% change in the homogenized axial stiffness parameter accuracy, indicating that the analysis of this model is affected more by the geometric approximation error than by the discretization error.

The second example consists of a base two satin weave composite [21]. The parameters used to construct the geometric model of this weave were taken from a series of micrographs of a representative sample of the composite. The design target bundle fraction was 0.55. The matrix material is an amorphous glass composed of silicon, oxygen, and carbon. The matrix was modeled as a transversely isotropic material with degraded properties to represent the through-thickness matrix cracks in the as-processed composite. The axial Young's and shear moduli of the matrix are 11.5 msi and 4.0 msi. The transverse Young's and shear moduli are 8.1 msi and 3.3 msi. The Poisson's ratio is 0.26. These values will be compared with specimen test data in future work [28]. The fibers are a ceramic material. The axial Young's and shear moduli of the fiber bundles are 16.6 msi and 6.55 msi. The transverse Young's and shear moduli of the fiber bundles are 16.2 msi and 6.52 msi. The Poisson's ratio of the bundles is 0.24.

Meshes of varying amounts of uniform refinement were generated within the constructed geometric model. The coarsest mesh, (Figure 14) contains 2,380 vertices and 11,050 elements, the mesh created with one level of refinement (Figure 15) contains 10,475 vertices and 52,509 elements, and the finest mesh (Figure 16) contains 62,436 vertices and 338,253 elements. Meshes of each of the three levels of uniform refinement were also generated with the mesh volume fraction corrected to within $\pm 0.5\%$ of the target volume fraction of 0.55. The mesh faces classified on the interior fiber bundle surfaces of each of the volume fraction corrected meshes are shown in Figure 17. The number of mesh vertices and mesh volume fraction data of all of the meshes are listed in Table 3.

Homogenization analyses were performed and the in-plane stiffness parameters were examined. For the modeled composite weave the in-plane fiber bundle directions correspond to the x and z axes, with the y axis normal to the plane of the composite.

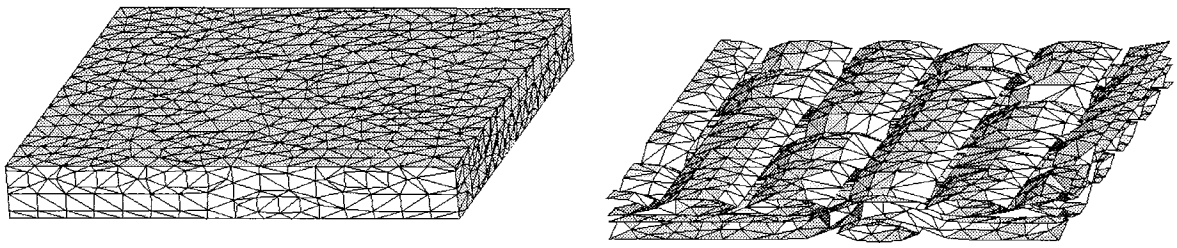

(a) (b)

Figure 14. Coarse mesh of base two satin weave model.
(a)External mesh faces. (b)Fiber bundle surface mesh faces.

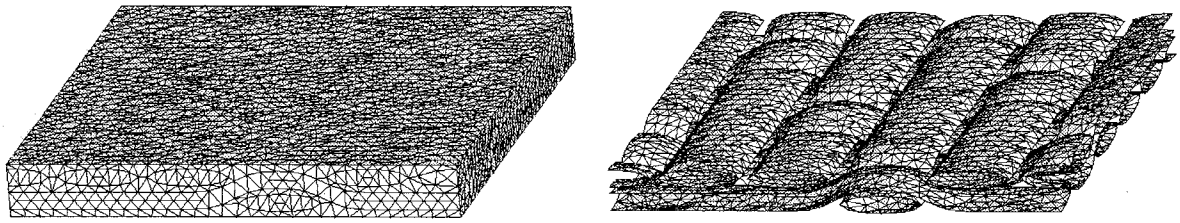

(a) (b)

Figure 15. Medium mesh of base two satin weave model.
(a)External mesh faces. (b)Fiber bundle surface mesh faces.

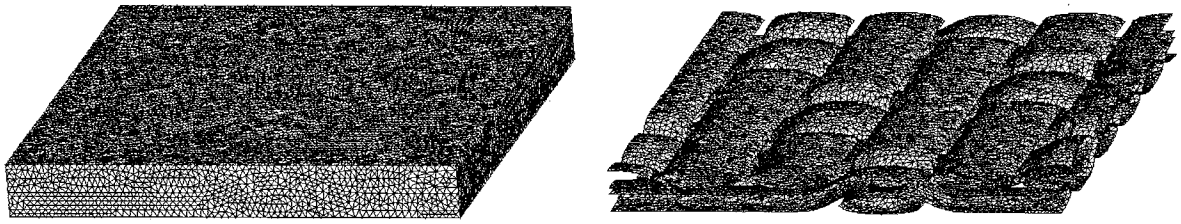

(a) (b)

Figure 16. Fine mesh of base two satin weave model.
(a)External mesh faces. (b)Fiber bundle surface mesh faces.

The in-plane material parameters are therefore the values of G_{11}, G_{33}, G_{55}, and G_{13}.

The homogenized stiffness parameters were compared to the values calculated using

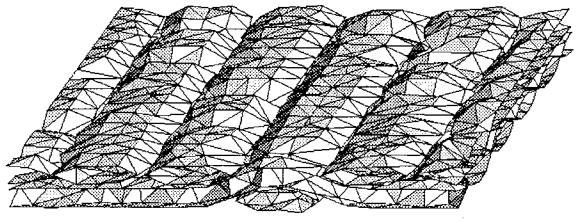

(a)

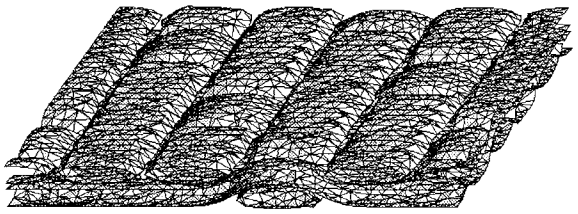

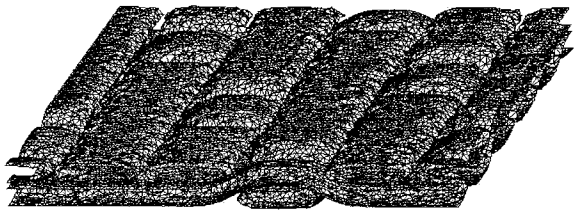

(b) (c)

Figure 17. Fiber bundle surface mesh faces of meshes corrected to 0.55 volume fraction. (a)Coarse mesh. (b)Medium mesh. (c)Fine mesh.

the finest discretization corrected to 0.17% C_b^{FE} error. The in-plane normal stiffness parameter data determined from these analyses are shown in Table 3, and the in-plane shear and Poisson effect stiffness parameter data are shown in Table 4. The values for the coarsest and finest discretizations differed by at most 1.64% when adjusted to within $\pm 0.5\%$ of the correct bundle volume fraction.

There is also little change in the stiffness parameters with large changes in the number of degrees of freedom in the model, indicating that the homogenization analysis is affected more by the amount of geometric approximation error than by the amount of the discretization error.

The results of this example again show that it is possible to achieve accurate homogenization results with coarse finite element discretizations if the C_c^{FE} values are adjusted to the correct values. The total CPU mesh generation and solving time required for the coarsest discretization was 44 times faster than the time required for the finest discretization.

Number of Vertices	Mesh Bundle Volume Fraction	Mesh Bundle Volume Fraction Error (%)	G_{11} ($\times 10^7$)	G_{11} Difference (%)	G_{33} ($\times 10^7$)	G_{33} Difference (%)
2,380	0.3905	-29.00	1.3099	-11.5	1.3085	-11.6
2,380	0.4460	-18.91	1.3651	-6.54	1.3636	-6.60
2,380	0.4593	-16.50	1.3783	-5.64	1.3769	-5.69
2,380	0.5526	0.47	1.4715	0.74	1.4688	0.60
10,475	0.4441	-19.25	1.3582	-7.01	1.3570	-7.05
10,475	0.4594	-16.5	1.3734	-5.97	1.3723	-6.00
10,475	0.5515	0.28	1.4649	0.29	1.4635	0.24
62,436	0.458	-16.7	1.3690	-6.28	1.3677	-6.31
62,436	0.5509	0.17	1.4607	0.0	1.4600	0.0

Table 3. Mesh sizes, mesh bundle volume fractions, and in-plane normal homogenized stiffness parameter values of the discretizations of the base two satin weave geometric model.

Number of Vertices	Mesh Bundle Volume Fraction Error (%)	G_{55} ($\times 10^6$)	G_{55} Difference (%)	G_{13} ($\times 10^6$)	G_{13} Difference (%)
2,380	-29.00	4.5536	-8.05	3.7119	-12.94
2,380	-18.91	4.7007	-5.07	3.9193	-8.08
2,380	-16.50	4.7387	-4.31	3.9694	-6.91
2,380	0.47	5.0334	1.64	4.3233	1.39
10,475	-19.25	4.6717	-5.66	3.8825	-8.94
10,475	-16.5	4.7115	-4.86	3.9399	-7.60
10,475	0.28	4.9753	0.47	4.2853	0.50
62,436	-16.7	4.6904	-5.28	3.9182	-8.11
62,436	0.17	4.9520	0.00	4.2639	0.00

Table 4. Mesh sizes, mesh bundle volume fraction errors, and in-plane shear and Poisson effect homogenized stiffness parameter values of the discretizations of the base two satin weave geometric model.

7. Determination of Local Stresses

A thorough analysis of a given composite weave must also include the calculation of the local stresses in the weave which result from loadings on the larger-scale homogenized material. These local values aid in the design of composite microstructure by indicating areas of high stress which may lead to failure of the composite. The meshes generated by the procedures described in this paper conform to the model geometry, and are therefore capable of producing reliable local stress data.

The local unit cell stresses corresponding to the strain field $\underline{\hat{\varepsilon}}$ existing at a given point in the larger–scale model are given by

$$\underline{\sigma_i} = \underline{A_i}\,\underline{\hat{\varepsilon}} \tag{28}$$

where $\underline{\sigma_i}$ are the stresses at the i^{th} integration point in the unit cell model, and $\underline{A_i}$ is the stress concentration matrix relating the strain field at a given point in the macroscopic model to the stresses at the i^{th} integration point in the unit cell model [12].

The following example of local stress calculation uses the base two satin weave composite unit cell of section 6. The homogenized material stiffness parameters were used to calculate $\underline{\hat{\varepsilon}}$ corresponding to a 100 ksi uniaxial stress in the x-direction. This direction corresponds to the warp direction of the unit cell.

The results of applying equation (28) to every integration point in the coarse mesh adjusted to 0.47% C_b^{FE} error (shown in Figure 17(a)) are shown in Figure 18. This figure represents an exploded view of the unit cell, with the groups of elements comprising the matrix (at the left), warp bundles (at the top), and weft bundles (at the bottom) separated for clarity. Linear elements were used for the homogenization analysis of this example, and the elements in this figure are colored according to the values of the maximum principal stress calculated at their single integration points. The correspondence between the colors and the stress values is shown by the color bar at the top of Figure 18.

The stresses in the warp bundles show concentration "bands" near the crossovers where the warp and weft bundles are woven together. This is due to the load carrying capacity of bundles being reduced when their axes do not align with the loading direction, and the load therefore being transferred to the neighboring bundles which are aligned in the loading direction. The matrix material shows bands of stress values due to additional reinforcement by the transverse stiffness of the weft bundles. The peak stress in the warp bundles is 148.0 ksi.

The medium mesh (Figure 17(b)) adjusted to 0.28% C_b^{FE} error was also analyzed to examine the effect on the peak stress. The local stresses calculated with the medium mesh (Figure 19) exhibit the same characteristics as the coarse mesh. The peak stress in the warp bundles is 160 ksi.

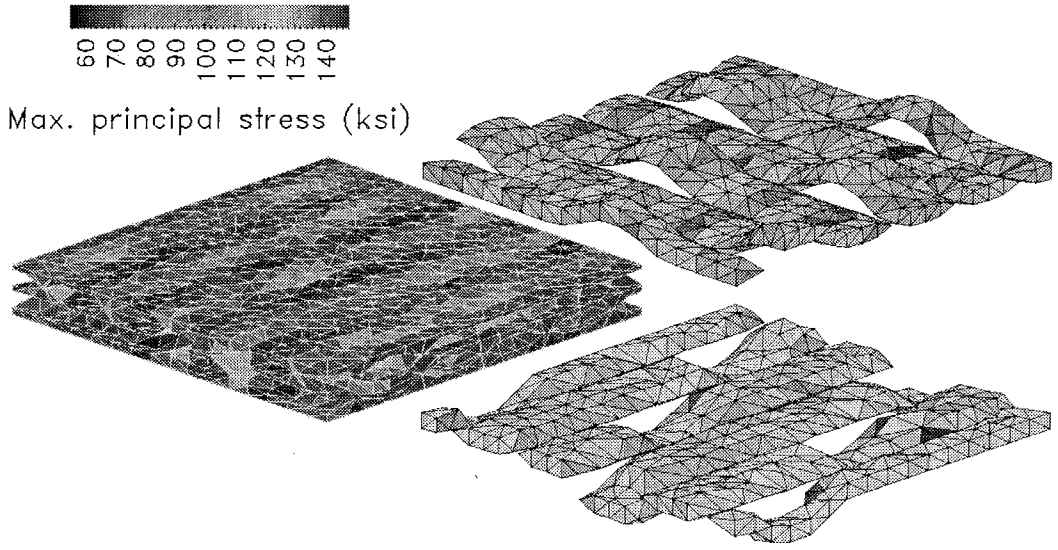

Figure 18. Maximum principal stress values in a base two satin weave composite resulting from a uniaxial x-direction stress of 100 ksi applied to the homogenized material (Coarse mesh). The peak stress in the warp bundles is 148.0 ksi

8. Conclusions

This paper presented a system for the efficient three-dimensional homogenization analyses of complex composite materials. These capabilities include a matched meshing algorithm which simplifies the specification of periodic boundary conditions, and an iterative solver algorithm capable of efficiently handling the multiple right hand sides required for homogenization analyses. An algorithm was also developed to correct the mesh volume fraction, and the effect of the mesh volume fraction error on the values of homogenized material stiffness parameters was shown to be greater than that of the discretization error. Acceptable homogenization results may therefore be obtained with coarse discretizations if the mesh volume fraction is controlled. The reliable calculation of local stresses permitted by the mesh conforming to the model geometry was also demonstrated.

9. Acknowledgments

The support of ARPA/ONR under grant number N00014–92J-1779, and of the Allison Advanced Development Company under the LC^3 project is gratefully acknowledged.

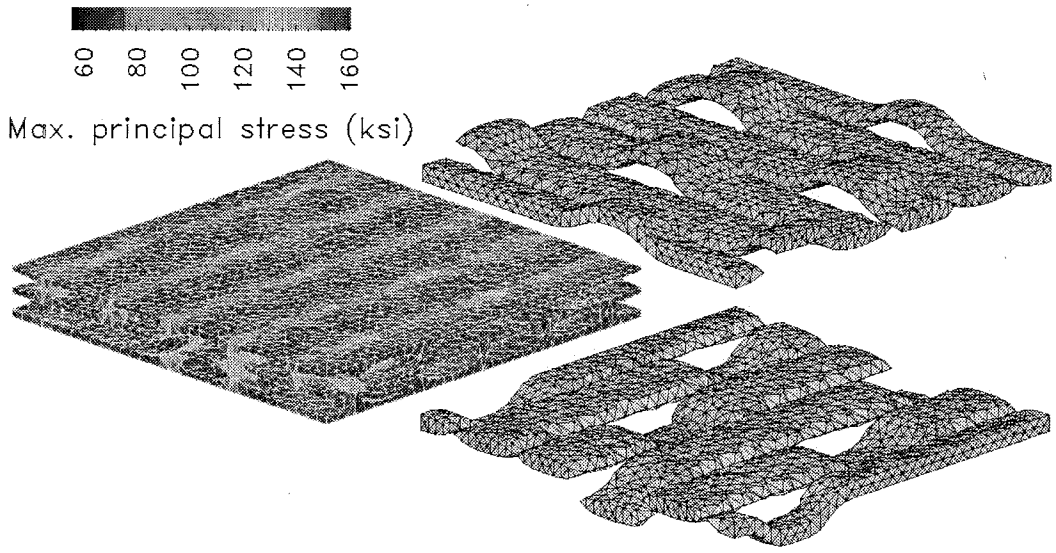

Figure 19. Maximum principal stress values in a base two satin weave composite resulting from a uniaxial x-direction stress of 100 ksi applied to the homogenized material (Medium mesh). The peak stress in the warp bundles is 160 ksi.

10. References

[1] M. W. Beall and M. S. Shephard. Mesh data structures for advanced finite element computations. Technical Report 19-1995, Scientific Computation Research Center, Rensselaer Polytechnic Institute, Troy, NY 12180-3590, 1995. submitted to Int. J. Num. Meth. Engng.

[2] A. Dasgupta, R. K. Agarwal, and S. M. Bhandarkar. Three-dimensional modeling of woven-fabric composites for effective thermo-mechanical and thermal properties. *Composites Science and Technology*, 56:209–223, 1996.

[3] H. L. de Cougny and M. S. Shephard. Surface meshing using vertex insertion. In *Proceedings of the 5th International Meshing Roundtable*, 1996.

[4] Hugues L. de Cougny, Mark S. Shephard, and Marcel K. Georges. Explicit node point smoothing within the Finite Octree mesh generator. Technical Report 10-1990, Scientific Computation Research Center, Rensselaer Polytechnic Institute, Troy, NY 12180-3590, 1990.

[5] Hugues L. de Cougny, Mark S. Shephard, and C. Ozturan. Parallel three-dimensional mesh generation on distributed memory MIMD computers. *Engineering with Computers*, 12(2):94–106, 1996.

[6] G. J. Dvorak and Y. Benveniste. On transformation strains and uniform fields in multiphase elastic media. *Proc. R. Soc. Lond.*, 437:291, 1992.

[7] D. A. Field. Laplacian smoothing and Delaunay triangulations. *Comm. Appl. Num. Meth.*, 4:709–712, 1987.

[8] J. Fish and V. Belsky. Multi-grid method for periodic heterogeneous media .2. multiscale modeling and quality control in multidimensional case. *Computer Methods in Applied Mechanics and Engineering*, 126:17–38, 1995.

[9] J. Fish and V. Belsky. Generalized aggregation multilevel solver. *Submitted to: Int. J. Numer. Meth. Engng.*, 1997.

[10] J. Fish, P. Nayak, and M. H. Holmes. Microscale reduction error indicators and estimators for a periodic heterogeneous medium. *Computational Mechanics: The International Journal*, 14:1–16, 1994.

[11] J. Fish and A. Suvorov. Automated adaptive multilevel solver. *Submitted to: Comp. Meth. Appl. Mech. Engng.*, 1997.

[12] Jacob Fish and Amir Wagiman. Multiscale finite element method for a locally nonperiodic heterogeneous medium. *Computational Mechanics*, 12:164–180, 1993.

[13] E. Hashin and Walter B. Rosen. The elastic moduli of fiber-reinforced materials. *Journal of Applied Mechanics, Transactions of the ASME*, pages 223–232, 1964.

[14] Behrooz Hassani. A direct method to derive the boundary conditions of the homogenization equation for symmetric cells. *Communications in Numerical Methods in Engineering*, 12:185–196, 1996.

[15] R. Hill. A self-consistent mechanics of composite materials. *Journal of the Mechanics and Physics of Solids*, 13:213, 1965.

[16] S. J. Hollister and N. Kikuchi. Homogenization theory and digital imaging: A basis for studying the mechanics and design principles of bone tissue. *Biotechnology and Bioengineering*, 43:586–596, 1994.

[17] M. Krizek. On the maximal angle condition for linear tetrahedral elements. *SIAM J. Numer. Anal.*, 29:513–520, 1992.

[18] M. Mäntylä. *Introduction to Solid Modeling*. Computer Science Press, Rockville, Maryland, 1988.

[19] T. Mori and K. Tanaka. Average stress in matrix and average elastic energy of materials with misfitting inclusions. *Acta Metallurgica*, 21:571–574, 1973.

[20] A. N. Norris. A differential scheme for the effective moduli of composites. *Mechanics of Materials*, 4, 1985.

[21] Ning Pan. Analysis of woven fabric strengths: Prediction of fabric strength under uniaxial and biaxial extensions. *Composites Science and Technology*, 56:311–327, 1996.

[22] W. J. Schroeder. *Geometric Triangulations: with Application to Fully Automatic 3D Mesh Generation*. PhD thesis, Rensselaer Polytechnic Institute, Scientific Computation Research Center, RPI, Troy, NY 12180-3590, May 1991. SCOREC Report # 9-1991.

[23] J. Shah. Conceptual development of form features and feature modellers. *Research in Engineering Design*, pages 93–108, 1991.

[24] M. S. Shephard. The specification of physical attribute information for engineering analysis. *Engineering with Computers*, 4:145–155, 1988.

[25] M. S. Shephard, J. E. Flaherty, H. L. de Cougny, C. Ozturan, C. L. Bottasso, and M. W. Beall. Parallel automated adaptive procedures for unstructured meshes. In *Parallel Computing in CFD*, volume R-807, pages 6.1–6.49. AGARD, Neuilly-Sur-Seine, France, 1995.

[26] M. S. Shephard and M. K. Georges. Reliability of automatic 3-D mesh generation. *Comp. Meth. Appl. Mech. Engng.*, 101:443–462, 1992.

[27] Earl W. Swokowski. *Calculus with Analytic Geometry*. Prindle, Weber and Schmidt, 1979.

[28] R. Wentorf, R. Collar, J. Fish, and M. S.Shephard. Influences of some constituent features on the homogenized mechanical properties of composite materials. *In Preparation*, 1997. Scientific Computation Research Center, Rensselaer Polytechnic Institute, Troy, NY.

[29] R. Wentorf, M. S. Shephard, G. J. Dvorak, J. Fish, M. W. Beall, R. Collar, and K.-L. Shek. Software framework for mechanism-based design of composite structures. In *Proceedings of the 21st Annual Cocoa Beach Conference on Composite Advanced Ceramics, Materials and Structures*, 1997. to appear.

[30] John Whitcomb, Kanthikannan Srirengan, and Clinton Chapman. Evaluation of homogenization for global/local stress analysis of textile composites. *Composite Structures*, 31:137–149, 1995.

[31] XOX Corporation, Two Appletree Square, Suite 334, Minneapolis, Minnesota 55425. *SHAPES Reference Manual, Release 2.0.8*, July 20, 1993.